Additive Manufacturing 27 (2019) 474–481

Contents lists available at ScienceDirect

Additive Manufacturing

journal homepage: www.elsevier.com/locate/addma

Full Length Article

A novel strategy to fabricate thin 316L stainless steel rods by continuous directed energy deposition in Z direction

Fei Weng[a], Shiming Gao[a], Jingchao Jiang[a,b], JianJian Wang[a,c], Ping Guo[d,*]

[a] Department of Mechanical and Automation Engineering, The Chinese University of Hong Kong, Hong Kong 999077, PR China
[b] Department of Mechanical Engineering, University of Auckland, Auckland 1142, New Zealand
[c] Shun Hing Institute of Advanced Engineering, The Chinese University of Hong Kong, Hong Kong, PR China
[d] Department of Mechanical Engineering, Northwestern University, Evanston, IL, 60208, USA

ARTICLE INFO

Keywords:
Continuous directed energy deposition
Z direction
316L
Stainless steel

ABSTRACT

Thin 316L stainless steel rods were fabricated by continuous directed energy deposition in Z direction. The process parameters (laser power, scan velocity, and powder feeding rate) were carefully selected to obtain a stable deposition process and the effects of powder feeding rate and scan velocity were studied. A preliminary study on microstructure and tensile properties of the specimens was carried out. Results indicated that the specimen showed superior austenite/ferrite (γ/δ) dual phase microstructure, high strength (608.24 MPa), and good plastic deformation capacity (65.08% shrinkage rate) when setting the laser power at 45.2 W, powder feeding rate at 2.81 g/min, and scan velocity at 0.5 mm/s. The technique reported in this paper is expected to lay the foundation for the deposition of wire or frame structures more efficiently than traditional layer-by-layer directed energy deposition.

1. Introduction

In recent decades, additive manufacturing (AM) has developed into a popular technique for fabricating components in a layer-by-layer manner [1–4]. Particularly, laser additive manufacturing (LAM) [5] shows great advantages in printing metal components and opens a wide array of new applications. The popular LAM techniques include selective laser sintering/melting (SLS [6]/SLM [7]) and directed energy deposition (DED) [8], corresponding to their respective material feeding methods: powder bed and synchronous powder feeding. Compared with SLS/SLM techniques, DED provides some unique process potentials, especially in the repair of worn components [9] and preparation of functional graded materials [10].

Various metal materials have been used for DED, including AISI 4340 steel [11], 316 L stainless steel (316 L SS) [12], Inconel 718 Ni-based alloy [13], Ni60 A Ni-based alloy [14], Ti-6Al-4 V titanium alloy [15], AlCoCrFeNi high-entropy alloy (HEA) [16], and some mixed powders for composite material preparation [17–19]. 316 L SS has been extensively used in DED research due to high strength, high ductility, and good formability [12,20–23]. The relevant research emphasis was generally put on the effect of deposition parameters or deposition strategies to obtain better part accuracy and properties. For example, Zhang et al. [23] investigated the effect of laser power, scan velocity, and powder feeding rate on the clad profile (height and width), microstructure, and mechanical properties. Wang et al. [20] studied the influence of deposition strategies and oblique angle on the properties of 316 L thin wall parts. It was found that parallel deposition strategy was more beneficial to the ultimate tensile strength (UTS) and elongation rate of the deposited specimens compared with the oblique deposition strategy. And a larger oblique angle led to higher UTS but lower elongation rate. Guo et al. [12] investigated the influence of building direction on the microstructure, mechanical properties and machinability of bulk stainless steel parts. Homogeneous microstructures were found at the building direction of 0° showing higher tensile strength and hardness, while massive larger dendritic grains were present in that of 90°. de Lima and Sankaré [24] reported the fabrication of high aspect ratio 316 SS stringers by DED with carefully selected process parameters. The influence of raw particle characteristics (e.g. particle size) on the DED specimen properties was also investigated by Boisselier et al. [25].

However, most of the reported studies in DED of 316 L SS are in a traditional layer-by-layer manner to fabricate thin-wall specimens or cubic solid components. It is challenging to fabricate the slender or frame structures in traditional layer-by-layer manner DED, owing to the frequent intermittent steps. It is favorable to fabricate the specimen in a continuous way without interruption between layers, just as the

* Corresponding author.
E-mail address: ping.guo@northwestern.edu (P. Guo).

https://doi.org/10.1016/j.addma.2019.03.024
Received 8 November 2018; Received in revised form 11 March 2019; Accepted 24 March 2019
Available online 31 March 2019
2214-8604/ © 2019 Published by Elsevier B.V.

continuous casting method [26]. In this case, the final deposited component will not be affected by the interfaces between layers. In Ref. [26], Dwivedi et al. reported an approach to fabricate uni-directional and branching slender structures by DED in a continuous manner. They proposed a mathematical model for the process planning for fabrication of slender structures and successfully prepared linear, spiral, and branched structures under suitable process parameters. The paper, however, put the emphasis on the verification of its mathematical model without further discussion on the microstructures and properties of printed parts.

Inspired by the studies mentioned above, thin 316 L SS rods were prepared by continuous directed energy deposition in Z direction (Z-DED) in this paper. Firstly, the process parameters were carefully selected to fabricate the rods with high dimensional accuracy in Z direction. Furthermore, the microstructure and mechanical properties of the rods were investigated extensively. This study is expected to lay foundation for the fabrication of wire or frame structures by continuous DED of 316 L SS or other functional materials.

2. Materials and experimental details

316L stainless steel plates with dimensions of 100 mm*100 mm*4 mm were used as the substrate. 316 L stainless steel powders in particle size of 20˜53 μm were used as the precursor material, supplied by *Sandvik* with the nominal composition listed in Table 1. The directed energy deposition equipment used in this paper was self-developed, the schematic and actual in-chamber setup of which are shown in Fig. 1.

The laser source is a 500 W multi-mode continuous-wave infrared laser with 1070-nm wavelength (YLR-500-MM-AC-Y14, *IPG Photonics*). The actual diameter of laser focal spot is around 300 μm. The powder feeder (GPV PF2/2) is supplied by *GTV Thermal Spray*. The 6 degree-of-freedom (DOF) platform is a PI H840.D11 hexapod stage along with a C-887 hexapod controller, both from *Physik Instrumente (PI)*. A co-axial ring nozzle COAX 40-F (*Fraunhofer ILT*) is attached to the laser cladding head. The cladding head is integrated by *Reis Lasertec*. Nitrogen gas with purity of 99.999% was used as both the carrier and nozzle cooling gas during the deposition. The focal diameter of the powder stream is around 400 μm. The flow rates were set at 3.0 L/min and 10 L/min for the carrier gas and the nozzle cooling gas, respectively. The whole setup is housed in a glove box for atmosphere control of the building environment.

In traditional DED, a single track or thin layer is deposited firstly in the X–Y plane, whereafter the next track or layer is deposited on the previous formed layer. Hence, the scan length (ΔX) is just equal to the deposition layer length (*L*), as shown in Fig. 2a. In this paper, the vertical rod specimens were deposited by the continuous Z-DED strategy with platform displacement only in Z direction (Fig. 2b and c). It is noteworthy that the process parameters should be strictly controlled to ensure a successful Z-DED. As shown in Fig. 2b, the deposition height (*H*) should match with Z direction displacement (*ΔZ*) of the platform in unit time. Only in this way, the deposition process can be stable and continuous, and the height of final specimen would be equal to the designed one. In the ideal condition, the actual deposition occurs at the focal plane (the dashed red line in Fig. 2) of both the laser beam and feeding powder stream. If the process parameters are not properly controlled, *H* would deviate from *ΔZ*, resulting in defocusing and even interruption of the Z-DED process. Fig. 2c shows an example of failed Z-DED when *H* is much lower than *ΔZ* resulting in large defocusing distance (*Δf*). The failure can be ascribed to low laser power, insufficient powder feeding rate, or high scan velocity.

Table 1
Nominal composition of the 316 L stainless steel powder (wt.%).

Alloy	Fe	C	Cr	Ni	Mo	Si	Mn	S	P
316 L	Bal.	0.03	17.0	12.0	2.5	0.7	1.5	0.03	0.04

A series of experiments were carried out to fabricate the vertical rods with designed length of 15 mm. The dimensions of deposited rods were measured by a digital caliper with accuracy of 0.01 mm. The selected specimens with their heights within the range of 15 ± 1 mm are listed in Table 2. The deposition lengths and diameters were 14.33˜15.50 mm and 1.16˜1.36 mm, respectively. Seen from Specimens S1-S3, the deposition height increases with the pace of increased powder feeding rate. However, the deposition diameter is lower under the largest powder feeding rate (Specimen S1). This can be attributed to the limited laser energy. To further increase the deposition height, higher laser power is used (Specimen S4-S6). Both the deposition height and diameter decrease along with the increased scan velocity. The deposited height accuracy was calculated ($\eta = |H\text{-}15|/15$) and listed in Table 2. It is obvious that specimen S5 shows the highest deposition height accuracy. With a well combination of laser power, scan velocity, and powder feeding rate, a vertical rod with high dimensional accuracy in Z direction can be obtained.

Phase constituents of the initial powders and the deposited rods were analyzed by X-ray diffractometer (Smartlab, *Rigaku*). Microstructures of the rods were observed by a high resolution optical microscope (RH-2000, *Hirox*). The samples for microstructure observation were prepared via standard metallurgical sample preparation route. The etchant was diluted aqua regia solution (50 vol.%). Tensile property of the deposited rods was tested by a universal testing machine (CMT4204, *MTS systems*). The tensile test was carried out at a constant stretching speed of 1.0 mm/min. The thin rod specimens were tested directly without machining. The UTS and shrinkage rates (Ψ) on transverse cross section of the tensile specimens were calculated accordingly.

3. Results and discussion

3.1. Phase constituent

Fig. 3 shows the XRD analysis results of raw powder and DED specimens. The raw powder is mainly comprised of face centered cubic (FCC) austenite phase (γ). The result corresponds to the intrinsic characteristics of 316 L SS, a kind of austenite steel [24]. However, partial body centered cubic (BCC) ferrite phase (δ) appears in the DED specimens (as shown in the dashed circle), just like the report on SLM of 316 L SS by Sun et al. [27] but different from some reports of mono γ phase in the DED specimens [23,28]. Compared with Refs [23]. and [28], the process parameters in the present paper are quite different, including the laser power, powder feeding velocity, scan velocity and spot size. The difference would result in different heating and cooling rate in the molten pool, and then different phase constituent is obtained. According to the report from Guo et al. [12], higher cooling rate leads to a fully austenitic microstructure due to the suppression of solute redistribution. In the present study, the sample is deposited in Z direction with limited contact area between sample and substrate. Hence, the heat conduct through substrate is restrained [29] and thus result in lower cooling rate.

According to the composition of Ni, Cr, and Fe, 316 L SS corresponds to a mono γ area at 650 °C (annotated by *A* in Fig. 4 [23]). However, it is not the case in non-equilibrium heating and cooling conditions of DED. During the DED process, the composition segregation is prone to occur in the molten pool due to uneven temperature distribution generated by laser beam [30], resulting in regional austenite instability. If the local composition drops into the two-region area of γ and δ, composite phase constituents will be obtained after rapid solidification. Hence both γ and δ phases appear in the XRD results (Fig. 3). The formation of δ-ferrite phase is beneficial to the mechanical properties of the 316 L SS specimens, especially the hot crack resistance [31].

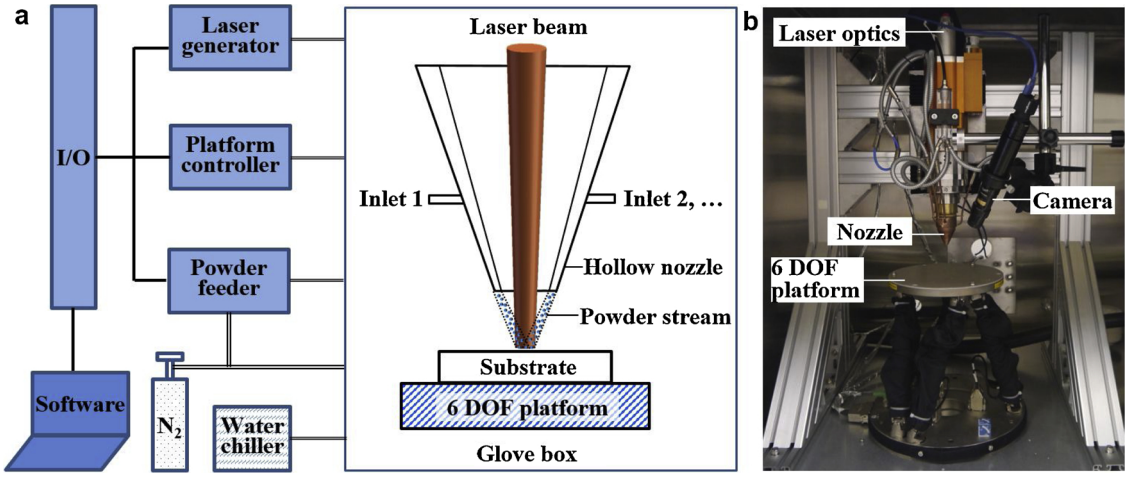

Fig. 1. (a) Schematic of the DED equipment; (b) actual experimental setup in the glove box.

3.2. Microstructure

Fig. 5 shows the morphologies of rod specimens after polishing. All the specimens exhibit continuous microstructure, but spherical defects (voids) appear in the deposited rods (Fig. 5d). However, no crack is spotted in specimens. The voids are generated from the carrier or chilling gas from the nozzle, or the evaporation of phases with low boiling point [32]. Marya et al. [21] reported similar phenomenon in the laser additive manufactured thin-walled air vent. The spherical voids, either at the micron or submicron scale, are attributed to solidification shrinkage just like that in welding technique. Except for spherical voids, some irregular defects appeared in specimen S2, as shown in the dashed circle (Fig. 5b). The irregular defects might be lack of fusion voids [33] or inclusions induced by oxidation or burning loss [34]. Either voids or inclusions are easy to cause stress concentration and detrimental to the mechanical properties.

Fig. 6 shows the microstructure of longitudinal cross section at the central position of rods after polishing and chemical etching. The microstructure is comprised of dominant austenite and intergranular skeletal ferrite. This corresponds well with the XRD results (Fig. 4). Besides, there are some intragranular dot-like phases, which are probably voids as mentioned above or metastable phases formed during DED as reported by Weiss and Stickler [35]. However, no carbides or intermetallic phases mentioned in Ref [35]. are picked out in the XRD results (Fig. 3), probably due to the low content. In the present work, the main microstructure of specimens is identified as austenite and ferrite dual phase structure. As seen in Figs. 6a-c, higher powder feeding rate leads to finer microstructure, since more powders take more energy away and induce higher cooling rate. Similarly, higher scan velocity also results in finer microstructure (Fig. 6d-f).

Table 2
Process parameters and dimensions of the deposited vertical rods.

No.	Power, W	Powder feeding rate, g/min	Scan velocity, mm/s	Height, mm	Height accuracy, %	Diameter, mm
S1	34.3	3.09	0.4	14.61	97.40	1.18
S2	34.3	2.81	0.4	14.42	96.13	1.20
S3	34.3	2.46	0.4	14.10	94.00	1.16
S4	45.2	2.81	0.4	15.50	96.67	1.36
S5	45.2	2.81	0.5	14.81	98.73	1.32
S6	45.2	2.81	0.6	14.33	95.53	1.28

It is interesting that different kinds of microstructures appear at different positions of the deposited rods, as shown in Fig. 7. The outer layer shows different microstructure from that of the internal position and there is a transition zone between them, as annotated in Fig. 7a, b, e, and f. The internal position shows a dual phase microstructure of dominant austenite and inter ferrite (Fig. 7c, d, and g) as mentioned earlier. However, the outer layer shows regular austenite grains (Fig. 7h). The diverse microstructure is attributed to the Gaussian energy distribution of the laser beam and different cooling conditions at different positions. It is reasonable to assume that the outer layer undergoes lower peak temperature compared with that of the internal position considering the Gaussian energy distribution of the laser beam. Moreover, the outer layer of rods undergoes a higher cooling rate due to the convective heat transfer with the ambient air and N_2. Therefore, the outer layer retains regular austenite grains after rapid cooling. In

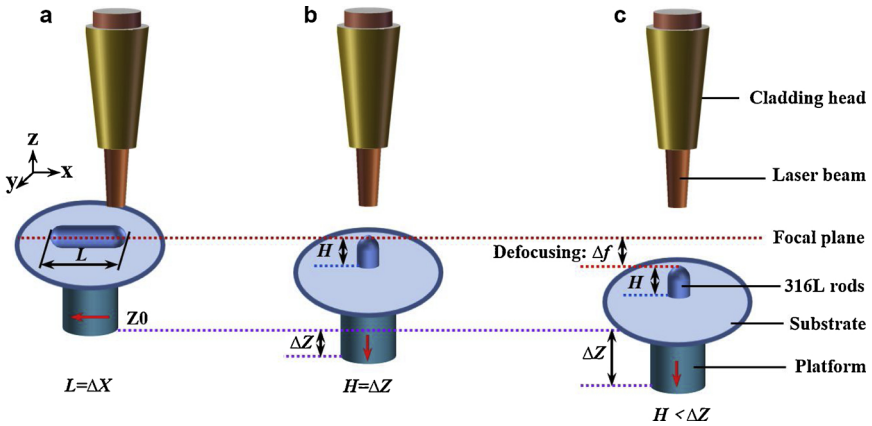

Fig. 2. (a) Traditional DED, scan length (ΔX) is equal to the deposition layer length (L); (b) successful Z-DED, deposition height (H) is equal to the displacement of the platform in Z direction (ΔZ); (c) one example of failed Z-DED, $H < \Delta Z$. Z0 is the initial position of platform. Red arrows: platform displacement direction. (For interpretation of the references to colour in this figure legend, the reader is referred to the web version of this article.).

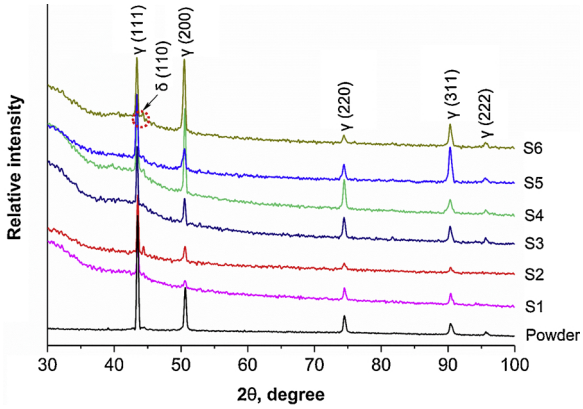

Fig. 3. XRD patterns of the initial 316 L stainless steel powder (powder) and the DED rods (S1-S6).

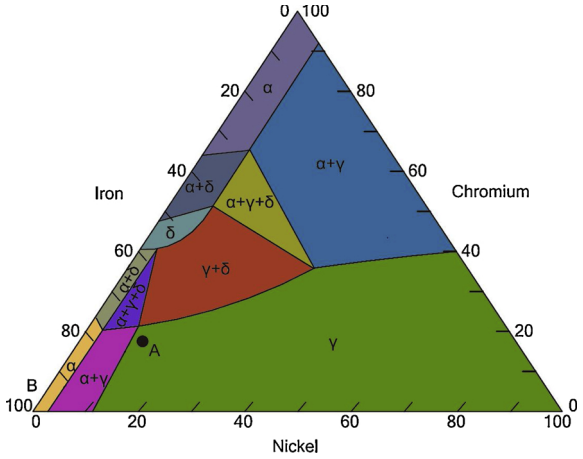

Fig. 4. Equilibrium phase diagram for Iron–Nickel–Chromium alloy system at 650 °C (*A* stands for the composition of initial 316 L powder) [23].

comparison, the internal position experiences lower cooling speed and the austenite phase has more time to decompose into ferrite, leading to the dual phase microstructure.

As mentioned previously, both cooling rate and potential composition segregation contribute to the formation of different microstructures. According to the study on welds from Wegrzyn [36], the welds were almost entirely austenitic with Cr_{eq}/Ni_{eq} between 1.0 and 1.3, while the welds were austenitic but contained a small quantity of ferrite with Cr_{eq}/Ni_{eq} between 1.3 and 1.6. Cr_{eq} and Ni_{eq} are chromium and nickel equivalents, which can be determined by the following two equations [36]:

$$Cr_{eq} = \%\ Cr + \%\ Mo + 1.5\%\ Si + 0.5\%\ Nb \quad (1)$$

$$Ni_{eq} = \%\ Ni + 35\%\ C + 20\%\ N \quad (2)$$

For 316 L SS, the ratio of Cr_{eq}/Ni_{eq} is 1.52 (within the range from 1.3 to 1.6). Thus, it is reasonable to obtain the dual phase microstructure. According to previous study [37], Cr is easier to be oxidized than Ni under the same condition. Therefore, partial Cr could be oxidized preferably on the specimen surface due to insufficient protective gas, which results in a lower Cr_{eq}/Ni_{eq} ratio less than 1.3 in the outer layer. Hence the appearance of single austenitic outer layer is reasonable.

3.3. Tensile property

Tensile test results of the vertical rods are shown in Fig. 8. The UTS and Ψ of the tensile specimens are annotated. Specimen S5 shows the highest UTS, followed by specimens S3, S1, S4 and S6, respectively. While, specimen S2 shows the lowest UTS. Moreover, specimen S5 shows relative high Ψ (65.08%). Hence, specimen S5 exhibits both high strength and plastic deformation capacity.

The changes of UTS and Ψ cannot be directly related to the process parameter settings, which could be attributed to the unstable deposition process under inappropriate process parameters. As aforementioned, the actual deposition height would be different from the designed dimension if the deposition rate lost stability. The unstable deposition process leads to different heating and cooling history, resulting in different microstructure and properties. Apart from the microstructure, the oxides formed on the specimen surface would act as defects and be detrimental to the tensile property. To sum up, specimen S5 shows the best height accuracy and highest UTS among the specimens in this paper.

In order to analyze the fracture mechanism, the fracture morphologies after tensile test were observed, as shown in Fig. 9. Results indicate that the fracture morphologies all show dimple fracture characteristics, a typical ductile fracture morphology. However, the dimple dimensions are different. According to the relevant theory of fracture mechanics, larger dimple dimensions (both in diameter and depth) mean better ductility. In comparison, specimens S5 and S6 show relative large dimples on the fracture surface, indicating better ductility. Though the fracture morphology of specimen S2 shows relative large dimples, the values of both UTS and Ψ are very low, which can be attributed to the spherical and irregular defects (Figs. 5 and 9b).

The UTS of specimen S5 (608.24 MPa) is, however, lower than that of 316 L SS components deposited using a layer-by-layer manner in DED. It was reported the UTS of deposited 316 L SS component could be as high as ~683 MPa [23]. The difference can be analyzed as follows:

(1) Since the process parameter windows are diverse, the results are not comparable due to the quite different heating and cooling history, as well as the final microstructure. In the present study, the laser power, powder feeding rate, and scan velocity were all in a low-value range, which were 34.3–45.2 W, 2.46–3.09 g/min, and 0.4-0.6 mm/s, respectively. Zhang et al. [23] reported the laser metal deposition shaping (LMDS) of 316 L SS under the parameter window of 600–1400 W, 4–20 g/min, and 2–10 mm/s.
(2) The defects (voids and inclusions) in the rods are unfavorable to the mechanical properties. In the future, more work will be carried out to eliminate the defects in the deposited rods. An inert gas atmosphere should be guaranteed and some auxiliary methods such as vibration assisted laser additive manufacturing [38] will be tried.
(3) In this paper, the as-deposited rods are directly used for tensile test without surface machining. The surface oxides and defects are also detrimental to the mechanical properties. Though non-standard tensile specimens are also used in relevant published papers, they are always sampled by electron discharged machining and show smoother surface than the as-deposited [24].

Even so, considering the dimensions of the rod specimens versus the mechanical property, they can also meet the application requirements in some potential occasions, such as support structure in DED of complex structures. Some spiral wire or frame structures can also be deposited by the novel continuous Z-DED technique more efficiently than the conventional intermittent layer-by-layer DED.

4. Conclusions and future works

In this paper, a novel Z-DED strategy was used to fabricate 316 L SS rods in a continuous way. Dual phase microstructure (γ/δ) was obtained and the appearance of δ was beneficial to the mechanical properties. The specimen exhibiting both high UTS and Ψ can be

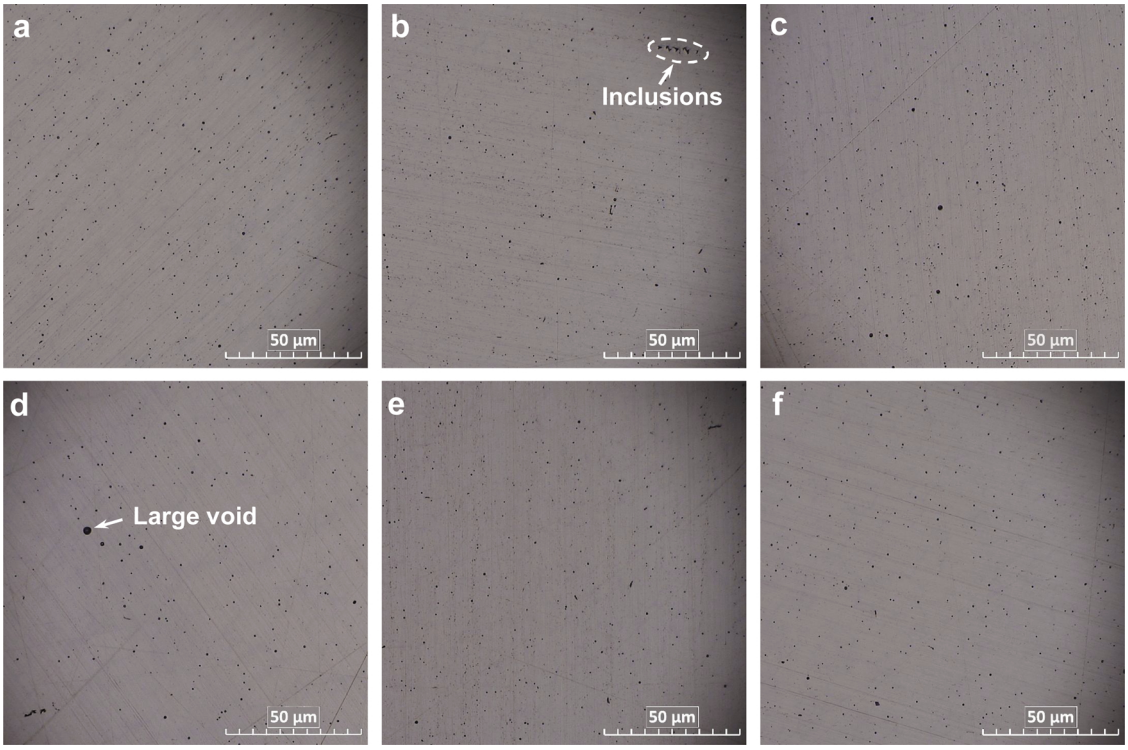

Fig. 5. Morphology of the transverse cross section of rods after polishing: (a) S1, (b) S2, (c) S3, (d) S4, (e) S5, and (f) S6.

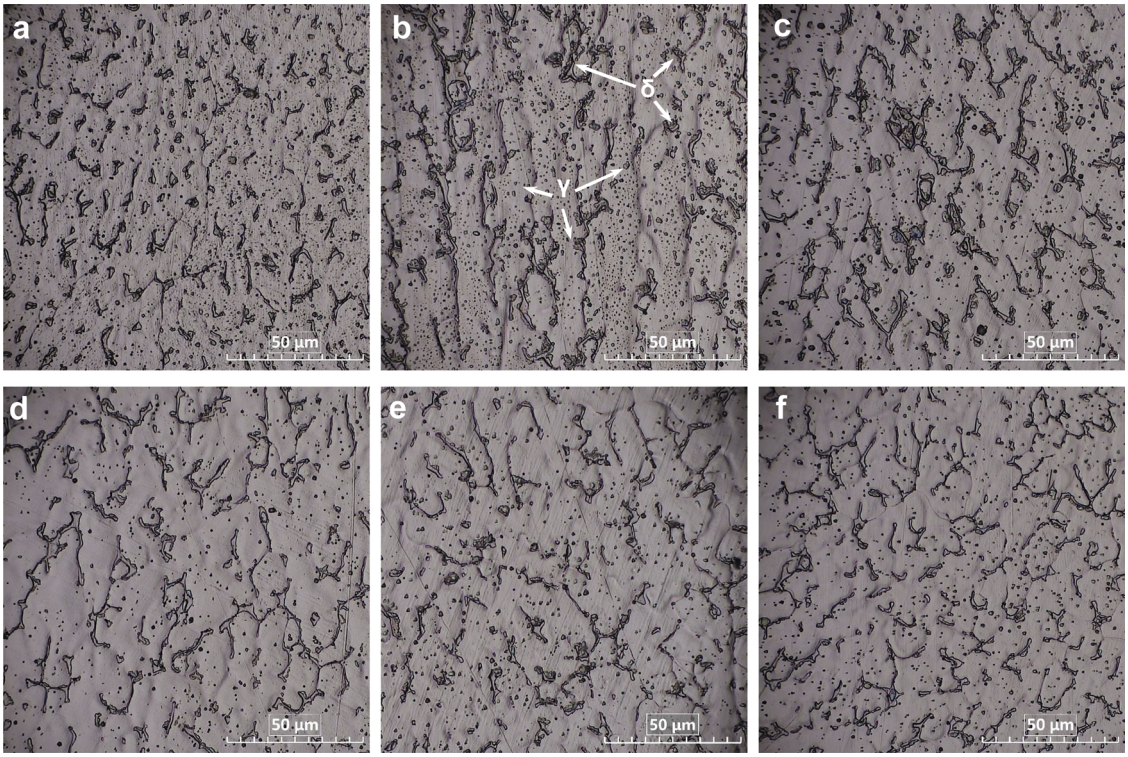

Fig. 6. Microstructure of the specimens at the central position of longitudinal cross section: (a) S1, (b) S2, (c) S3, (d) S4, (e) S5, and (f) S6.

obtained with carefully selected process parameters. The thin rods can be used as support structures during DED of complex bulk components. Based on the novel continuous Z-DED, direct deposition of thin spiral wire and even complex frame structures are expected to be accomplished with appropriate tilt of the platform.

The emphasis of future study should be put on the elimination of surface and inner defects of the specimens. Moreover, formation mechanism of the dual phase microstructure will be further clarified, as well as the effect of γ/δ ratio on the mechanical properties. Furthermore, rods with superior mechanical properties are expected to be fabricated by tailoring the microstructure.

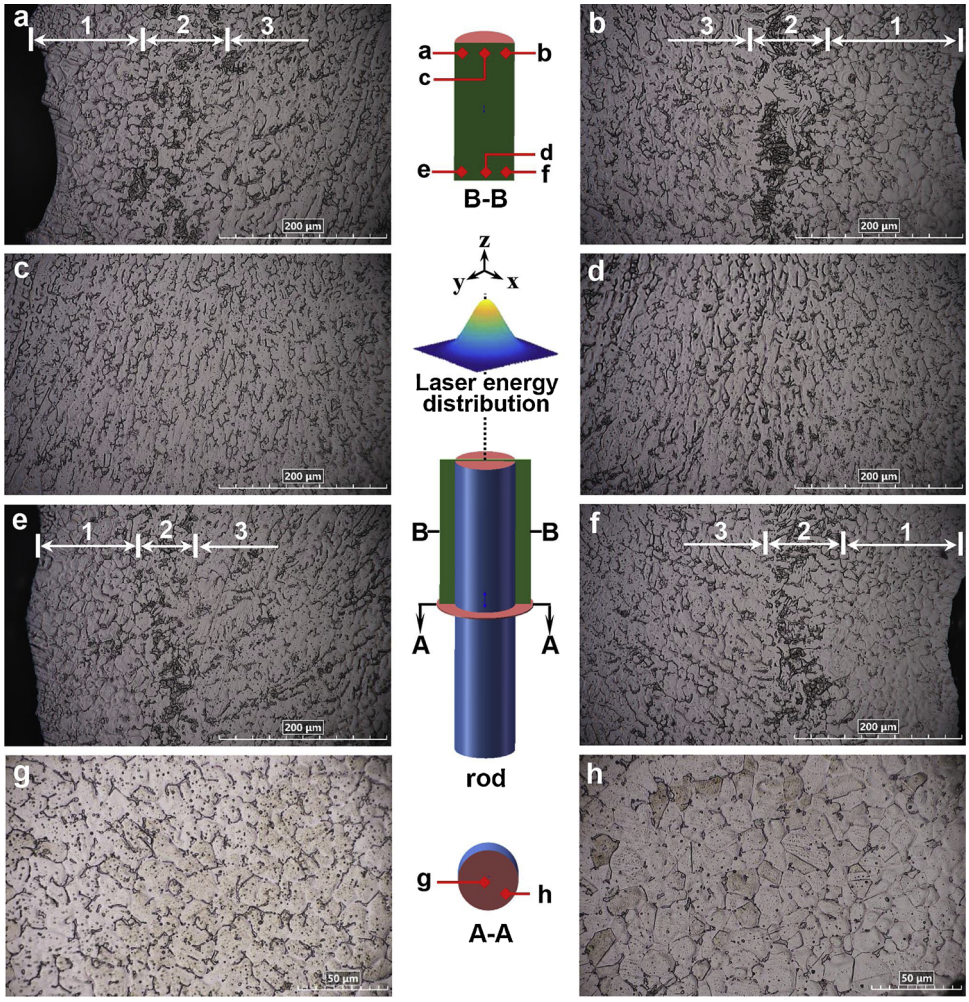

Fig. 7. Microstructure of different positions in specimen S5 (1, 2, 3 in a, b, e, f present: 1-outer layer, 2-transition zone, 3-internal position). The deposited rods (˜15 mm) were cut into two equal parts, and the upper part was sectioned longitudinally. The lower part was mounted to observe the transversal section. The sampling positions of a–h are annotated accordingly.

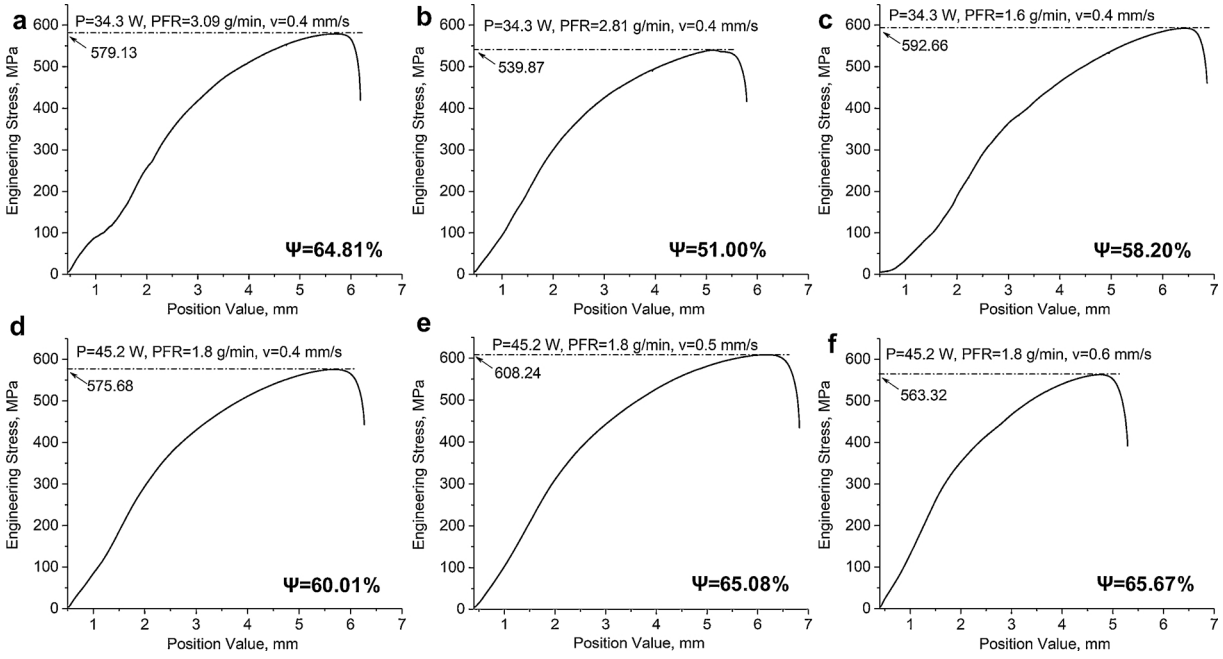

Fig. 8. Tensile engineering stress curves of the specimens deposited under different process parameters: (a) S1, (b) S2, (c) S3, (d) S4, (e) S5, and (f) S6.

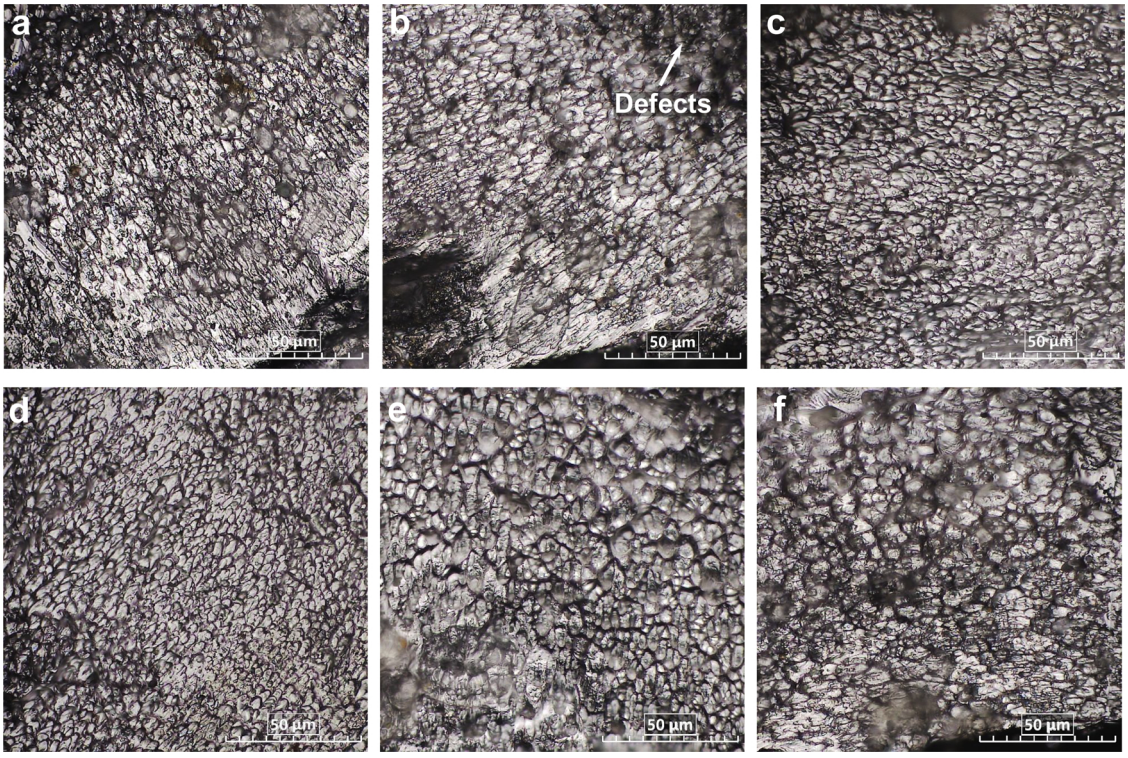

Fig. 9. Tensile fracture morphologies of the specimens: (a) S1, (b) S2, (c) S3, (d) S4, (e) S5, and (f) S6.

Acknowledgements

This work has been supported by the Shun Hing Institute of Advanced Engineering, CUHK, #RNE-p4-17; and the start-up fund provided by the McCormick School of Engineering, Northwestern University, Evanston, USA.

Appendix A. Supplementary data

Supplementary material related to this article can be found, in the online version, at doi:https://doi.org/10.1016/j.addma.2019.03.024.

References

[1] C.R. Cunningham, J.M. Flynn, A. Shokrani, V. Dhokia, S.T. Newman, Invited review article: strategies and processes for high quality wire arc additive manufacturing, Addit. Manuf. 22 (2018) 672–686.
[2] J. Jiang, J. Stringer, X. Xu, R.Y. Zhong, Investigation of printable threshold overhang angle in extrusion-based additive manufacturing for reducing support waste, Int. J. Comput. Integ. M. 31 (2018) 961–969.
[3] J. Jiang, X. Xu, J. Stringer, Support structures for additive manufacturing: a review, J. Manuf. Mater. Process. 2 (2018) 64.
[4] A. Bandyopadhyay, K.D. Traxel, Invited review article: metal-additive manufacturing—modeling strategies for application-optimized designs, Addit. Manuf. 22 (2018) 758–774.
[5] M. Schmidt, M. Merklein, D. Bourell, D. Dimitrov, T. Hausotte, K. Wegener, L. Overmeyer, F. Vollertsen, G.N. Levy, Laser based additive manufacturing in industry and academia, CIRP Ann. 66 (2017) 561–583.
[6] A. Cerardi, M. Caneri, R. Meneghello, G. Concheri, M. Ricotta, Mechanical characterization of polyamide cellular structures fabricated using selective laser sintering technologies, Mater. Design 46 (2013) 910–915.
[7] V. Cain, L. Thijs, J. Van Humbeeck, B. Van Hooreweder, R. Knutsen, Crack propagation and fracture toughness of Ti6Al4V alloy produced by selective laser melting, Addit. Manuf. 5 (2015) 68–76.
[8] M. Akbari, R. Kovacevic, An investigation on mechanical and microstructural properties of 316LSi parts fabricated by a robotized laser/wire direct metal deposition system, Addit. Manuf. 23 (2018) 487–497.
[9] P. Kattire, S. Paul, R. Singh, W. Yan, Experimental characterization of laser cladding of CPM 9V on H13 tool steel for die repair applications, J. Manuf. Process. 20 (Part 3) (2015) 492–499.
[10] Q. Lai, R. Abrahams, W. Yan, C. Qiu, P. Mutton, A. Paradowska, M. Soodi, Investigation of a novel functionally graded material for the repair of premium hypereutectoid rails using laser cladding technology, Compos. Part B Eng. 130 (2017) 174–191.
[11] G. Sun, R. Zhou, J. Lu, J. Mazumder, Evaluation of defect density, microstructure, residual stress, elastic modulus, hardness and strength of laser-deposited AISI 4340 steel, Acta Mater. 84 (2015) 172–189.
[12] P. Guo, B. Zou, C. Huang, H. Gao, Study on microstructure, mechanical properties and machinability of efficiently additive manufactured AISI 316L stainless steel by high-power direct laser deposition, J. Mater. Process. Tech. 240 (2017) 12–22.
[13] C. Zhong, N. Pirch, A. Gasser, R. Poprawe, J.H. Schleifenbaum, The influence of the powder stream on high-deposition-Rate laser metal deposition with inconel 718, Metals Basel 7 (2017) 443.
[14] L. Ri-sheng, S. Shao-ni, L. Zi-sheng, The influence of scanning methods on the cracking failure of thin-wall metal parts fabricated by laser direct deposition shaping, Eng. Fail. Anal. 59 (2016) 269–278.
[15] M. Gharbi, P. Peyre, C. Gorny, M. Carin, S. Morville, P. Le Masson, D. Carron, R. Fabbro, Influence of various process conditions on surface finishes induced by the direct metal deposition laser technique on a Ti–6Al–4V alloy, J. Mater. Process. Tech. 213 (2013) 791–800.
[16] I. Kunce, M. Polanski, K. Karczewski, T. Plocinski, K.J. Kurzydlowski, Microstructural characterisation of high-entropy alloy AlCoCrFeNi fabricated by laser engineered net shaping, J. Alloys. Compd. 648 (2015) 751–758.
[17] M. Zhong, W. Liu, Y. Zhang, X. Zhu, Formation of WC/Ni hard alloy coating by laser cladding of W/C/Ni pure element powder blend, Int. J. Refract. Metals Hard Mater. 24 (2006) 453–460.
[18] M.S. Domack, J.M. Baughman, Development of nickel-titanium graded composition components, Rapid Prototyping J. 11 (2005) 41–51.
[19] P.C. Collins, R. Banerjee, H.L. Fraser, The influence of the enthalpy of mixing during the laser deposition of complex titanium alloys using elemental blends, Scripta Mater. 48 (2003) 1445–1450.
[20] X. Wang, D. Deng, M. Qi, H. Zhang, Influences of deposition strategies and oblique angle on properties of AISI316L stainless steel oblique thin-walled part by direct laser fabrication, Opt. Laser Technol. 80 (2016) 138–144.
[21] M. Marya, V. Singh, S. Marya, J.Y. Hascoet, Microstructural development and technical challenges in laser additive manufacturing: case study with a 316L industrial part, Metall. Mater. Trans. B (2015) 1–12.
[22] G.T. Gray Iii, V. Livescu, P.A. Rigg, C.P. Trujillo, C.M. Cady, S.R. Chen, J.S. Carpenter, T.J. Lienert, S.J. Fensin, Structure/property (constitutive and spallation response) of additively manufactured 316L stainless steel, Acta Mater. 138 (2017) 140–149.
[23] K. Zhang, S. Wang, W. Liu, X. Shang, Characterization of stainless steel parts by Laser Metal Deposition Shaping, Mater. Design 55 (2014) 104–119.
[24] M.S.F. de Lima, S. Sankaré, Microstructure and mechanical behavior of laser additive manufactured AISI 316 stainless steel stringers, Mater. Design 55 (2014) 526–532.

[25] D. Boisselier, S. Sankaré, Influence of powder characteristics in laser direct metal deposition of SS316L for metallic parts manufacturing, Phys. Procedia 39 (2012) 455–463.
[26] R. Dwivedi, S. Zekovic, R. Kovacevic, A novel approach to fabricate uni-directional and branching slender structures using laser-based direct metal deposition, Int. J. Mach. Tools Manuf. 47 (2007) 1246–1256.
[27] Z. Sun, X. Tan, S.B. Tor, W.Y. Yeong, Selective laser melting of stainless steel 316L with low porosity and high build rates, Mater. Design 104 (2016) 197–204.
[28] P. Ganesh, R. Giri, R. Kaul, P. Ram Sankar, P. Tiwari, A. Atulkar, R.K. Porwal, R.K. Dayal, L.M. Kukreja, Studies on pitting corrosion and sensitization in laser rapid manufactured specimens of type 316L stainless steel, Mater. Design 39 (2012) 509–521.
[29] J. Song, Y. Chew, L. Jiao, X. Yao, S.K. Moon, G. Bi, Numerical study of temperature and cooling rate in selective laser melting with functionally graded support structures, Addit. Manuf. 24 (2018) 543–551.
[30] I.A. Roberts, C.J. Wang, R. Esterlein, M. Stanford, D.J. Mynors, A three-dimensional finite element analysis of the temperature field during laser melting of metal powders in additive layer manufacturing, Int. J. Mach. Tools Manuf. 49 (2009) 916–923.
[31] G. Lothongkum, E. Viyanit, P. Bhandhubanyong, Study on the effects of pulsed TIG welding parameters on delta-ferrite content, shape factor and bead quality in orbital welding of AISI 316L stainless steel plate, J. Mater. Process. Tech. 110 (2001) 233–238.
[32] F. Verhaeghe, T. Craeghs, J. Heulens, L. Pandelaers, A pragmatic model for selective laser melting with evaporation, Acta Mater. 57 (2009) 6006–6012.
[33] T. DebRoy, H.L. Wei, J.S. Zuback, T. Mukherjee, J.W. Elmer, J.O. Milewski, A.M. Beese, A. Wilson-Heid, A. De, W. Zhang, Additive manufacturing of metallic components – process, structure and properties, Prog. Mater. Sci. 92 (2018) 112–224.
[34] F. Weng, C. Chen, H. Yu, Research status of laser cladding on titanium and its alloys: a review, Mater. Design 58 (2014) 412–425.
[35] B.F. Weiss, R. Stickler, Phase instabilities during high temperature exposure of 316 austenitic stainless steel, Metall. Trans. 3 (1972) 851–866.
[36] T. Wegrzyn, Delta ferrite in stainless steel weld metals, Weld. Int. 6 (1992) 690–694.
[37] F. Weng, H. Yu, C. Chen, K. Wan, High-temperature oxidation behavior of Ni-based superalloys with Nb and Y and the interface characteristics of oxidation scales, Surf. Interface Anal. 47 (2015) 362–370.
[38] W. Cong, F. Ning, A fundamental investigation on ultrasonic vibration-assisted laser engineered net shaping of stainless steel, Int. J. Mach. Tools Manuf. 121 (2017) 61–69.